# Evaluation and statistical inference for human connectomes

Franco Pestilli[1], Jason D Yeatman[1], Ariel Rokem[1], Kendrick N Kay[1,2] & Brian A Wandell[1]

**Diffusion-weighted imaging coupled with tractography is currently the only method for *in vivo* mapping of human white-matter fascicles. Tractography takes diffusion measurements as input and produces the connectome, a large collection of white-matter fascicles, as output. We introduce a method to evaluate the evidence supporting connectomes. Linear fascicle evaluation (LiFE) takes any connectome as input and predicts diffusion measurements as output, using the difference between the measured and predicted diffusion signals to quantify the prediction error. We use the prediction error to evaluate the evidence that supports the properties of the connectome, to compare tractography algorithms and to test hypotheses about tracts and connections.**



Magnetic resonance (MR) diffusion imaging methods and tractography algorithms estimate the trajectories of white-matter fascicles (tracts) in the human brain *in vivo*[1–3]. Because these measurements are obtained *in vivo*, they can be used to clarify the relationship between the tract tissue properties and behavior, cognition and development as well as to identify disease biomarkers. Experimental measurements combining behavior and diffusion imaging show that tissue properties of specific tracts are correlated with a range of cognitive abilities. The properties of these tracts change during development and in response to experience. For example, changes in tissue properties are correlated with developmental progress, language, cognition, decision making, disease and trauma[4–9].

The collection of white-matter tracts and connections is called the connectome[10,11]. Tractography algorithms use diffusion-weighted images to derive many fascicles that comprise the candidate connectome. Conventional tractography generates fascicles one at a time; however, these algorithms do not assess how well the full connectome predicts the diffusion data. Thus, a key limitation of current practice concerns how to establish confidence in the connectome and specific fascicles within the connectome, considering that selecting different parameters or different algorithms produces substantially different candidate connectomes[12–14] (**Fig. 1** and **Supplementary Fig. 1**). To be able to evaluate connectomes derived with different methods, it is important to assess the strength of the evidence supporting each of these models.

We introduce a method that refines a candidate connectome containing many potentially unsubstantiated fascicles to an optimized connectome. Fascicles are retained in the optimized connectome only if they are needed to predict the diffusion data. We show that the optimized connectome predicts the diffusion data accurately and analyze the properties of the optimized connectome. Finally, we introduce methods that evaluate the strength of the evidence concerning specific tracts and connections.

## RESULTS

### Deriving an optimized connectome with LiFE

We developed the LiFE algorithm to evaluate how well a candidate connectome obtained through tractography methods fits the underlying white-matter diffusion data. The method solves a set of simultaneous linear equations (**Supplementary Fig. 2** and Online Methods) to estimate a weight for each fascicle; this weight describes the fascicle's contribution toward predicting the diffusion data. These equations are solved by non-negative linear least-squares algorithms[15]. Only fascicles with positive weight are retained (Online Methods and **Supplementary Fig. 2e**). This connectome evaluation is global, as the fascicles in the optimized connectome all contribute to predicting the diffusion data measured in the whole white-matter volume.

The LiFE method can be applied to candidate connectomes created with any number of fascicles, parameter settings and tractography algorithms. It identifies the subset of fascicles that are supported by the diffusion data.

### Prediction accuracy of the optimized connectome

We evaluated the prediction accuracy of candidate and optimized connectomes using cross-validation (**Fig. 2**). To illustrate the LiFE methodology, we acquired and analyzed two different data sets from adult human brains. We obtained data set STN150 using 150 angles and 2-mm$^3$ spatial resolution, with a diffusion sensitization value, $b$, of 2,000 s/mm$^2$ ($n$ = 1 brain, two repeats). Data set STN96 includes 96 diffusion directions at 1.5 mm$^3$, with a $b$ value of 2,000 s/mm$^2$ ($n$ = 6 brains, two repeats each). We also used data obtained from the Human Connectome Project (HCP90, utilizing 90 diffusion directions at 1.25 mm$^3$, with a $b$ value of 2,000 s/mm$^2$). In the examples here and below, we

[1]Department of Psychology, Stanford University, Stanford, California, USA. [2]Department of Psychology, Washington University in St. Louis, St. Louis, Missouri, USA. Correspondence should be addressed to F.P. (franco.pestilli@stanford.edu).

RECEIVED 2 MAY; ACCEPTED 8 AUGUST; PUBLISHED ONLINE 7 SEPTEMBER 2014; DOI:10.1038/NMETH.3098

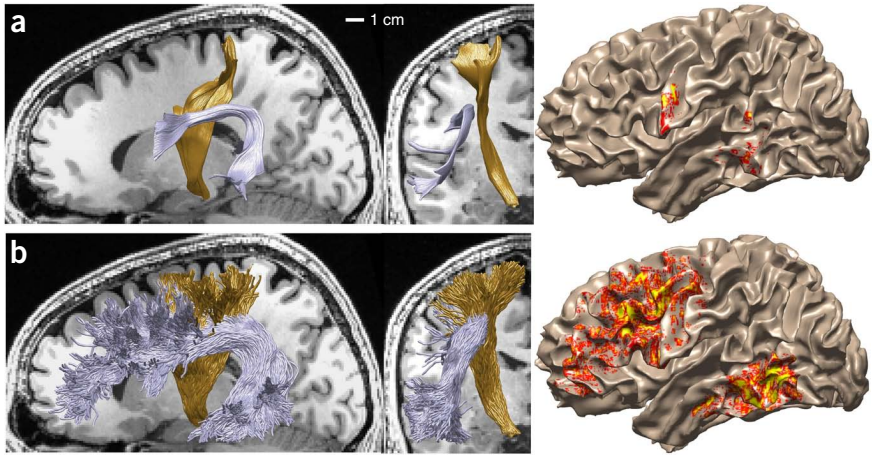


**Figure 1** | Tract trajectory estimates and cortical projection zones from different tractography algorithms. (**a**) Deterministic tractography. Sagittal and coronal views of the arcuate fasciculus (purple) and corticospinal tract (gold) in a candidate connectome generated using deterministic tractography. The density with which the fiber projects onto the cortical surface is indicated by the color overlay. Yellow indicates highest fiber density. (**b**) Probabilistic tractography. Images as in **a** except for a candidate connectome generated using probabilistic tractography.

generated whole-brain candidate connectomes using constrained spherical deconvolution (CSD)-based probabilistic tractography[16] (using a maximum harmonic order, $L_{max}$, of 10 and $5 \times 10^5$ seeds). In each case, the candidate connectome contains 500,000 fascicles.

We measured and predicted the diffusion modulation, i.e., the diffusion relative to the mean isotropic signal in each voxel (**Fig. 2** and **Supplementary Fig. 3a**,**b**). Two independent data sets (repeats), $D_1$ and $D_2$, were collected in each brain and data set (STN150 and STN96) (**Fig. 2a**). We tracked and estimated the fascicle weights that best fit $D_1$. Then we used the connectome and the estimated weights from $D_1$ to predict the diffusion signal in $D_2$ using the LiFE algorithm (**Fig. 2b**). The r.m.s. error between the prediction and $D_2$, which measures prediction error, was uniformly distributed across the white matter (**Fig. 2c**).

We compared the model prediction to the test-retest reliability of the data, which is the r.m.s. error between the two data sets, $D_{rmse}$. The model prediction error ($M_{rmse}$) is the r.m.s. error between the connectome prediction and $D_2$. We compared the model and test-retest reliability at each voxel using the ratio $R_{rmse} = M_{rmse}/D_{rmse}$. When $R_{rmse}$ is below 1, the model predicts $D_2$ more accurately than $D_1$ predicts $D_2$. Indeed, more than 70% of the voxels had an $R_{rmse}$ less than 1 (**Fig. 2d** and **Supplementary Fig. 3c**,**d**). In conclusion, the optimized connectome model predicted the second data set more accurately than assuming that the second data set equals the first.

## Optimized connectome fascicle properties

The candidate and optimized connectomes included more short (1–5 cm) than long (10 cm) fibers (**Fig. 3a** and **Supplementary Fig. 4a**). Histology shows[17,18] that there are even more short fibers below 1 cm, but these are not predicted by tractography models. Optimizing the connectome reduced the count in long and short fascicles approximately equally.

The number and values of positive weights in the optimized connectome depends on the spatial resolution, angular resolution and signal-to-noise ratio (SNR) of the acquired data. The number of positive weights for STN96 and STN150 was about 95,000 for both. For all three data sets (STN150, STN96 and HCP90), the fascicle weight distribution was approximately symmetric on a log-weight axis, with a large range of assigned weights (five log-units; **Fig. 3b**). Some fascicles contributed more to the predictions than others, and their weights were as much as two orders of magnitude greater.

Axon density varies across the white matter. For example, in the corpus callosum the axon density varies by a factor of 1.3 (ref. 19). If we consider only the axons with a diameter greater than 3 µm, this factor can be as large as 30 (ref. 19). Yet, typical candidate connectomes can vary by a factor of 300 or more[20] (**Fig. 3c**,**d** and **Supplementary Fig. 4b**). This exceeds the range observed in biological material, but principled methods

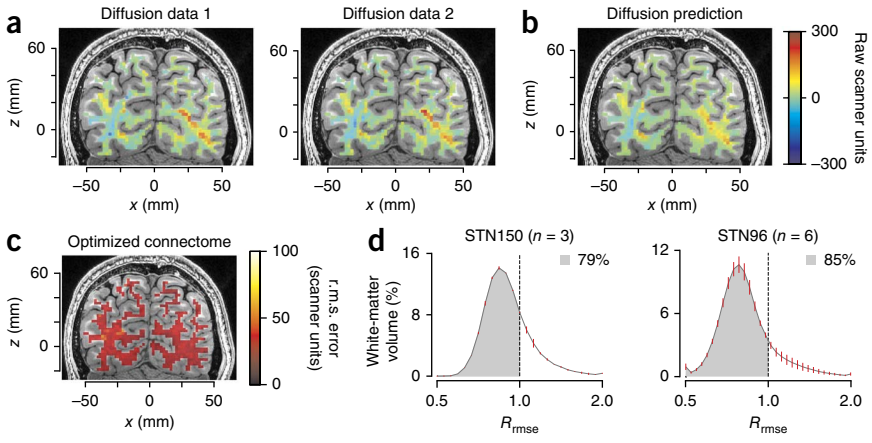


**Figure 2** | Measured and predicted diffusion data and LiFE model prediction accuracy. (**a**) Maps of measured diffusion modulation (diffusion data 1 and 2: $D_1$ and $D_2$, respectively, in the main text) in a typical coronal brain slice and for a single diffusion direction. (**b**) Map of predicted diffusion modulation by LiFE (synthetic MRI signal; equation (7)) for the same brain slice and diffusion direction as in **a**. Connectome generated with CSD-based probabilistic tractography with $L_{max}$ = 10 and the STN150 data set ($n$ = 1 brain). (**c**) Distribution of LiFE model r.m.s. error: A representative coronal brain slice is shown. The color overlay shows the cross-validated model error ($M_{rmse}$) for the CSD-based probabilistic tractography with $L_{max}$ = 10 using the STN150 data set. (**d**) Histograms of the percentage of white-matter volume with a given $R_{rmse}$ for the STN150 and STN96 data sets. Error bars indicate ±1 s.e.m. across brains.

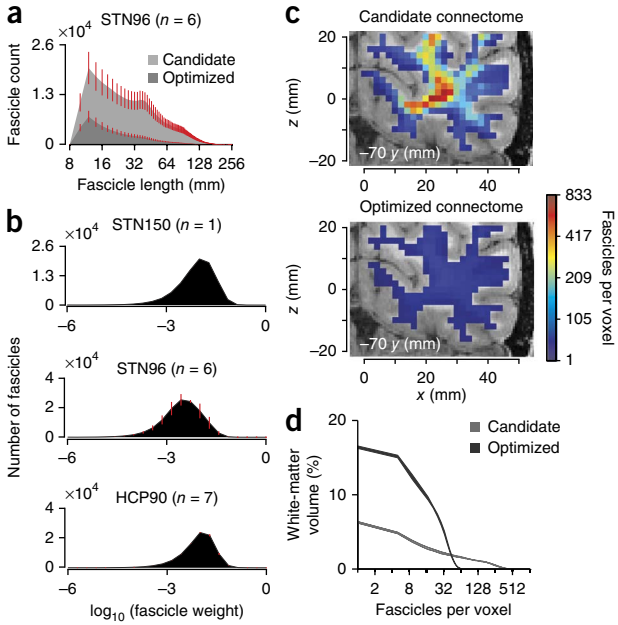


**Figure 3** | Properties of the LiFE connectome solution. (**a**) Fascicle length distribution. The histogram of fascicle length for candidate and optimized connectomes (STN96 data set, probabilistic CSD, $L_{max}$ = 10) was averaged across 6 brains. (**b**) Distribution of fascicle weights. Top, weights for a single connectome for the STN150 data set. Center, weights averaged across 6 connectomes for the STN96 data set. Bottom, weights averaged across 7 connectomes for the HCP90 data set. These connectomes contain two large portions of the left and right occipital and temporal lobes (Online Methods). Error bars indicate ±1 s.e.m. across brains. (**c**) Fiber density maps. Maps for the candidate and optimized connectomes are overlaid on a coronal brain slice (STN150). (**d**) Candidate and optimized connectome fascicle density histogram. A fiber density histogram for the candidate and optimized connectomes (STN96) is shown. Line width indicates ±1 s.d. across 6 brains.

may bring the dynamic range of the fascicles into biologically plausible ranges[20–22].

The fascicle density of the optimized connectome was close to a biologically plausible level (**Fig. 3d**). The optimized connectome had a smaller dynamic range because more than 50% of the fibers in the core of the white matter were eliminated. In contrast, the number of fascicles per voxel in the white matter adjacent to the cortex remained stable.

Naturally, any change in the power of the data—such as reducing the number of directions, making the sample size coarser or decreasing the SNR—will affect how many of the fascicles are supported by the measurements and thus retained in the optimized connectome. This is an important characteristic of the procedure as it allows the evaluation of the acquisition parameters that are needed to measure specific tracts (**Supplementary Fig. 4c**).

## Comparing connectome models

Using LiFE, we can compare the prediction error of optimized connectomes derived from different tractography methods. No single tractography method is optimal for all data acquisition protocols. Hence it is crucial to have a method that selects the optimal algorithm for particular data sets and research questions.

To illustrate this problem, we used LiFE to compare connectome models obtained with two tractography methods: a tensor-based deterministic algorithm[16,23,24] and a probabilistic tractography approach based on CSD with $L_{max}$ = 10 (STN150, STN96 and HCP90; refs. 16,25,26). The resulting connectomes were very different (**Fig. 1** and **Supplementary Fig. 1**). An important difference is that the probabilistic candidate connectome spanned the entire white-matter volume, whereas the deterministic connectome spanned about 80% of the voxels in the white-matter volume.

Next, we compared the voxelwise prediction error (r.m.s. error) from the optimal probabilistic and deterministic connectomes (**Fig. 4a**). In the voxels without any fascicles from the deterministic connectome, we set the diffusion signal prediction to an isotropic diffusion signal. For more than 70% of the voxels, the r.m.s. error was higher for the tensor-based deterministic algorithm than for the CSD-based probabilistic algorithm (**Fig. 4b**), a result suggesting that tensor-based deterministic algorithms do not capitalize on all the information present in the data.

We used a bootstrap method[27] to quantify the strength of the evidence showing that the mean r.m.s. error of the probabilistic connectome is smaller than the mean r.m.s. error of the deterministic connectome (**Fig. 4c**). We resampled (with replacement) the distribution of r.m.s. error values and computed the mean r.m.s. error of each resample. The distribution of mean r.m.s. error

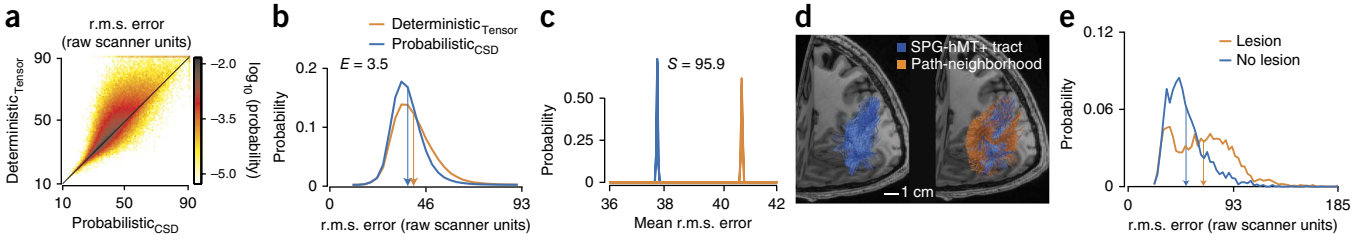


**Figure 4** | Comparison of connectome models, and the virtual lesion method. (**a**) Voxelwise prediction error. Error is shown for whole-brain probabilistic (CSD, $L_{max}$ = 10) and tensor-based deterministic optimized connectomes. Each white-matter voxel has a cross-validated r.m.s. error for both the optimal probabilistic and deterministic connectomes. The scatter-density plot compares these two values. (**b**) Distribution of r.m.s. error for probabilistic (CSD, $L_{max}$ = 10) and tensor-based deterministic optimized connectomes. The mean of each distribution is marked by vertical arrows. The Earth Mover's Distance (*E*) quantifies the lower error for the probabilistic model. (**c**) Representative bootstrap distribution of the mean r.m.s. error. *S* indicates the strength of the evidence favoring the probabilistic connectome over the deterministic connectome. Plots in **a**–**c** are for 1 brain, data set STN96. (**d**) Novel pathway connecting the motion-sensitive area hMT+ and the superior parietal gyrus (SPG) identified using a virtual lesion. Left, white-matter fascicles intersecting hMT+ and SPG in the left hemisphere of one individual brain. Right, path-neighborhood: fascicles sharing voxels with the SPG-hMT+ tract. (**e**) Distribution of r.m.s. error for lesioned and unlesioned models.

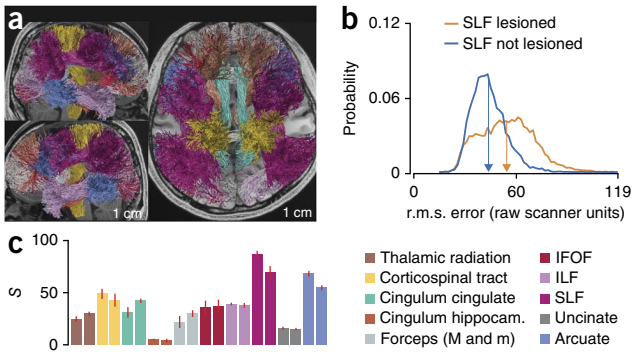


**Figure 5** | Major white-matter fascicles are supported by LiFE. (**a**) Twenty major human white-matter tracts in the optimized connectome (STN96, CSD probabilistic, $L_{max}$ = 10). (**b**) Distribution of cross-validated r.m.s. error of the optimized connectome ($F$), and the lesioned optimized connectome without the superior lateral fasciculus (SLF; $F' = F - f$). (**c**) Mean strength of the evidence ($S$) across 5 brains for each of the 20 major tracts shown in **a**. Bar location matches hemisphere (left and right, respectively). IFOF, inferior fronto-occipital fasciculus; ILF, inferior lateral fasciculus; M, forceps major; m, forceps minor. Error bars indicate ±1 s.e.m. across brains.

values for the deterministic algorithm was higher than that for the probabilistic algorithm. We summarized the strength of the evidence, $S$, for one model versus the other by using a measure of distance between these two distributions. We calculated the distance as the difference in the two means ($\mu$) divided by their pooled s.d. ($\sigma$).

$$S = \frac{\mu_D - \mu_P}{\sqrt{\sigma_D^2 + \sigma_P^2}}$$

The values $\mu_D$, $\sigma_D^2$ and $\mu_P$, $\sigma_P^2$ are the bootstrapped means and variances of the r.m.s. error for deterministic and probabilistic connectomes, respectively. The denominator is a conservative upper-bound estimate of the s.d. of the distribution of mean r.m.s. error pooled between deterministic and probabilistic connectomes[28]. The distance between the means, $S$, was on the order of 90 s.d. units. This strongly indicates that the mean r.m.s. error of the probabilistic connectome is smaller than that of the deterministic connectome for this data set and instrument. This result was consistent across data sets (**Supplementary Fig. 5**), thereby suggesting that probabilistic tracking may often be more accurate than deterministic tracking.

In addition to the mean r.m.s. error, we can compare the complete r.m.s. error distributions of the two models (**Fig. 4b**). We evaluated three additional metrics to compare r.m.s. error distributions—the Earth Mover's Distance[29] ($E$), Kullback-Leibler divergence and Jeffrey's divergence (**Supplementary Fig. 6**)—and found that $S$ and $E$ were both informative and reliable across a range of experimentally plausible conditions. Hence, we use these two measures for statistical evidence.

### The virtual lesion method: evidence for a brain connection

Next, we used the connectome model to assess the strength of the evidence supporting the existence of specific tracts that connect different brain regions.

The LiFE algorithm requires that fascicles in the optimized connectome contribute to the data prediction. Thus, removing any fascicle from the optimized connectome increases model prediction error. The impact on this error depends on the number and weights of the removed fascicles. We use the magnitude of the error increase to measure the strength of the evidence supporting the existence of any specific set of fascicles. We describe the analysis of fascicle removal as a 'virtual lesion'.

Here we illustrate a virtual lesion using an example tract connecting the superior parietal gyrus (SPG) and human motion-sensitive area hMT+[30,31]. First, we created a candidate connectome using MRtrix ($L_{max}$ = 10; 1,500,000 fibers). Second, we identified all fascicles terminating in the SPG and hMT+. Third, we identified the path-neighborhood of the fascicle[13]. More specifically, $f$ is the set of fascicles under test in the optimized connectome: for example, the SPG-hMT+ tract (**Fig. 4d**). The fascicle passes through a set of white-matter voxels, $v(f)$. The collection of all the other fascicles that pass through at least one of the voxels in $v(f)$ is the path-neighborhood of $f$. We refer to the path-neighborhood as $F$ (**Fig. 4d**). Only the fascicles in $F$ contribute to the model prediction of the diffusion signal in $v(f)$.

We measured the strength of the evidence in favor of the existence of the fascicles, $f$, using a bootstrap method[27]. We calculated the r.m.s. error of the predicted diffusion signal in each voxel, $v(f)$, using the path-neighborhood, $F$ (unlesioned model). We then calculated the r.m.s. error using a model in which we remove the fascicles in $f$, $F' = F - f$ (lesioned model). Next, we compared the r.m.s. error distributions for the path-neighborhood $v(f)$ for the lesioned and unlesioned model (**Fig. 4e**). We performed the analysis for additional subjects, reporting the mean values for $S$ and $E$ across subjects for data set HCP90 (**Supplementary Fig. 7**).

The analysis supports the existence of a white-matter tract between the SPG and hMT+, which has not yet been reported in humans. The tract is contained within the larger vertical occipital fasciculus[32,33]. This anatomical evidence in the living brain is consistent with functional data and post-mortem dissections in human[34–36] and macaque[30,31,37].

### LiFE confirmed 20 major white-matter tracts

To further validate the strength of the LiFE algorithm in evaluating connectomes, we calculated the strength of the evidence in favor of the existence of each of 20 long tracts that are known to exist in the human brain[3] ($n$ = 5 brains). The $S$ and $E$ values strongly supported the existence of all 20 major tracts (**Fig. 5** and **Supplementary Fig. 8**).

Further, these 20 tracts comprise 12 left-right pairs. In each case, the strength of the evidence supporting the corresponding left and right tract was similar and approximately consistent with their size. The superior lateral fasciculus (SLF) and arcuate are both large tracts, and there were more data supporting their existence. The uncinate and cingulum projecting to the hippocampus are smaller, and, correspondingly, the $S$ values for these tracts were smaller. The strength of evidence computed using $S$ depends on the size of the tract, the characteristics of the data acquisition (for example, SNR) and the effect of the lesion, whereas $E$ depends only on the data and the lesion effect size (**Supplementary Figs. 6** and **8**). This analysis validates LiFE by showing that it confirms the existence of known white-matter tracts.

Tractography is widely used to estimate the matrix of connections between major brain structures. We show that, when

LiFE optimizes the connectome, this matrix may change (**Supplementary Fig. 9**). The illustrated case concerns an interesting potential connection between primary visual cortex and the anterior commissure.

## DISCUSSION

### Connectome generation

A large set of diffusion measurements and tractography algorithms can predict white-matter fascicles (**Supplementary Table 1**). Each algorithm generates connectomes using its own set of theoretical principles and heuristics, and the choice of parameters and algorithms has a substantial effect on the tract estimates (**Fig. 1**). LiFE can be applied to the white-matter tracts from any tractography algorithm and measures the strength of the evidence supporting the existence of specific candidate tracts.

Tractography estimates can miss a real fascicle or generate a fascicle that does not exist (a 'false alarm'). The LiFE method reduces false alarms (**Fig. 3**). However, because LiFE is not a tractography algorithm, it does not supply missing tracts. Consequently, when using LiFE, investigators should begin with comprehensive candidate connectomes that are created to minimize misses but tolerate false alarms.

### Global tractography

The first algorithms for tractography were deterministic, local and greedy[38]. Following this early work, probabilistic formulations were introduced to account for uncertainty[16,25,26]. Also, nonlocal algorithms that operate on more than a single voxel at a time were proposed[39–43]. Most tractography algorithms combine connectome generation with indirect evaluation[39–41].

Sherbondy *et al.*[43,44] suggested separating connectome generation and evaluation algorithms. This separation enables investigators to measure the accuracy of predictions derived from different global tractography algorithms and to measure the accuracy of connectomes in predicting diffusion data. The principle of separating connectome generation and evaluation was adopted recently[45].

Global tractography algorithms can be further subdivided into two types: fascicle global and connectome global. Most global tractography algorithms are global in the sense that they consider constraints to path generation computed over entire fascicles. However, they do not constrain path generation over the complete connectome[39–41,44]. The principal goal of fascicle-global algorithms is to impose a degree of smoothness on the fascicle path. Connectome-global algorithms generate paths by constraining entire connectomes[21,43]. As the goal of these algorithms is path generation, they do not provide mechanisms for evaluating tractography solutions. LiFE provides a computational algorithm and a statistical inference framework that can evaluate virtually any connectome against the measured diffusion data.

### Connectome model validation

The most common approach to connectome validation is to compare tractography with another method. First, validation can be performed qualitatively by comparing tract estimates in individual *ex vivo* brains using both diffusion tractography and histology[46,47]. This method has various limitations. It is time consuming, the neural tissue is distorted and shrunk during the histological preparation, and the method can be applied to only a few cubic millimeters of white-matter volume of a single pathway[48]. Second, tractography estimates from probabilistic tractography *in vivo* also can be compared with blunt dissection in *ex vivo* specimens. For example, the overall shape and length of the optic radiation obtained with probabilistic tractography in living brains agree well with estimates obtained using *ex vivo* data[44]. Third, tractography algorithms are evaluated using artificially constructed physical or simulated phantoms of the fibers[49–51].

Using a separate method to confirm the existence of tracts is helpful for establishing general confidence in tractography. But this approach does not assess the strength of the evidence in a specific data set. For example, it is valuable to know that a tract estimated in one subject is also found in an *ex vivo* brain measurement. But it is fundamental to measure the degree of support for the presence or absence of a specific tract if anatomical changes are suspected, for instance, upon radiation therapy or if a tumor is present. LiFE establishes confidence about tracts and data obtained with specific instruments and subjects rather than relying on related measurements made with other instruments, methods and specimens.

Using LiFE, investigators can compare the accuracy of different connectomes and quantify the support in the data for specific tracts. New computational methods in quantitative MR imaging (MRI) will clarify the tissue properties of these tracts[52]. Taken together, the measurements and algorithms are helping us to build a complete model of the locations, organization and tissue properties of the human connectome.

LiFE is available as **Supplementary Software** and at https://francopestilli.github.io/life/.

## METHODS

Methods and any associated references are available in the online version of the paper.

*Note: Any Supplementary Information and Source Data files are available in the online version of the paper.*


### ACKNOWLEDGMENTS

We thank M.L. Perry for assistance with collecting and preprocessing the data and M. Ben-Shachar, R. Dougherty, J. Gardner, S. Ling, A. Mezer, A. Sherbondy, J. Winawer, H. Takemura, J. Solomon, L. Guibas, A. Butscher, C.Y. Zheng, R. Tibshirani and T. Hastie for useful comments and discussions. This work was funded by NEI F32 EY022294 from the US National Institutes of Health (NIH) to A.R. and by US National Science Foundation grant BCS1228397 to B.A.W. Data were provided in part by the Human Connectome Project, WU-Minn Consortium (D. Van Essen and K. Ugurbil, 1U54MH091657 NIH).


### AUTHOR CONTRIBUTIONS

F.P., J.D.Y. and B.A.W. designed the theoretical approach. F.P. implemented the approach and wrote the software, with help from A.R. and B.A.W. F.P. designed and implemented the statistical approach and the virtual lesion method. A.R., F.P. and J.D.Y. collected the data. K.N.K. advised on algorithms and statistics. F.P. and B.A.W. wrote the manuscript.

### COMPETING FINANCIAL INTERESTS

The authors declare no competing financial interests.




1. Zhang, Y. *et al.* Atlas-guided tract reconstruction for automated and comprehensive examination of the white matter anatomy. *Neuroimage* **52**, 1289–1301 (2010).
2. Yendiki, A. *et al.* Automated probabilistic reconstruction of white-matter pathways in health and disease using an atlas of the underlying anatomy. *Front. Neuroinform.* **5**, 23 (2011).

3. Yeatman, J.D., Dougherty, R.F., Myall, N.J., Wandell, B.A. & Feldman, H.M. Tract profiles of white matter properties: automating fiber-tract quantification. *PLoS ONE* **7**, e49790 (2012).
4. Yeatman, J.D., Dougherty, R.F., Ben-Shachar, M. & Wandell, B.A. Development of white matter and reading skills. *Proc. Natl. Acad. Sci. USA* **109**, E3045–E3053 (2012).
5. Samanez-Larkin, G.R., Levens, S.M., Perry, L.M., Dougherty, R.F. & Knutson, B. Frontostriatal white matter integrity mediates adult age differences in probabilistic reward learning. *J. Neurosci.* **32**, 5333–5337 (2012).
6. Thomason, M.E. & Thompson, P.M. Diffusion imaging, white matter, and psychopathology. *Annu. Rev. Clin. Psychol.* **7**, 63–85 (2011).
7. Lebel, C., Walker, L., Leemans, A., Phillips, L. & Beaulieu, C. Microstructural maturation of the human brain from childhood to adulthood. *Neuroimage* **40**, 1044–1055 (2008).
8. Scholz, J., Klein, M.C., Behrens, T.E.J. & Johansen-Berg, H. Training induces changes in white-matter architecture. *Nat. Neurosci.* **12**, 1370–1371 (2009).
9. Hoeft, F. *et al.* Neural systems predicting long-term outcome in dyslexia. *Proc. Natl. Acad. Sci. USA* **108**, 361–366 (2011).
10. Sporns, O., Tononi, G. & Kötter, R. The human connectome: a structural description of the human brain. *PLoS Comput. Biol.* **1**, e42 (2005).
11. Hagmann, P. *et al.* MR connectomics: principles and challenges. *J. Neurosci. Methods* **194**, 34–45 (2010).
12. Craddock, R.C. *et al.* Imaging human connectomes at the macroscale. *Nat. Methods* **10**, 524–539 (2013).
13. Wedeen, V.J. *et al.* The geometric structure of the brain fiber pathways. *Science* **335**, 1628–1634 (2012).
14. Catani, M., Bodi, I. & Dell'Acqua, F. Comment on "The geometric structure of the brain fiber pathways". *Science* **337**, 1605 (2012).
15. Kim, D., Sra, S. & Dhillon, S.I. A non-monotonic method for large-scale nonnegative least squares. *Optim. Methods Softw.* **28**, 1012–1039 (2013).
16. Tournier, J.-D., Calamante, F. & Connelly, A. MRtrix: diffusion tractography in crossing fiber regions. *Int. J. Imaging Syst. Technol.* **22**, 53–66 (2012).
17. Markov, N.T. *et al.* Cortical high-density counterstream architectures. *Science* **342**, 1238406 (2013).
18. Braitenberg, V. & Schuz, A. *Cortex: Statistics and Geometry of Neuronal Connectivity* (Springer, 1998).
19. Aboitiz, F., Scheibel, A.B., Fisher, R.S. & Zaidel, E. Fiber composition of the human corpus callosum. *Brain Res.* **598**, 143–153 (1992).
20. Sherbondy, A.J., Rowe, M.C. & Alexander, D.C. MicroTrack: an algorithm for concurrent projectome and microstructure estimation. *Med. Image Comput. Comput. Assist. Interv.* **13**, 183–190 (2010).
21. Smith, R.E., Tournier, J.-D., Calamante, F. & Connelly, A. SIFT: spherical-deconvolution informed filtering of tractograms. *Neuroimage* **67**, 298–312 (2013).
22. Bastiani, M., Shah, N.J., Goebel, R. & Roebroeck, A. Human cortical connectome reconstruction from diffusion weighted MRI: the effect of tractography algorithm. *Neuroimage* **62**, 1732–1749 (2012).
23. Basser, P.J., Pajevic, S., Pierpaoli, C., Duda, J. & Aldroubi, A. *In vivo* fiber tractography using DT-MRI data. *Magn. Reson. Med.* **44**, 625–632 (2000).
24. Lazar, M. *et al.* White matter tractography using diffusion tensor deflection. *Hum. Brain Mapp.* **18**, 306–321 (2003).
25. Behrens, T.E.J. *et al.* Non-invasive mapping of connections between human thalamus and cortex using diffusion imaging. *Nat. Neurosci.* **6**, 750–757 (2003).
26. Parker, G.J.M., Haroon, H.A. & Wheeler-Kingshott, C.A.M. A framework for a streamline-based probabilistic index of connectivity (PICo) using a structural interpretation of MRI diffusion measurements. *J. Magn. Reson. Imaging* **18**, 242–254 (2003).
27. Efron, B. & Tibshirani, R.J. *An Introduction to the Bootstrap* (Chapman & Hall, 1993).
28. Green, D.M. & Swets, J.A. *Signal Detection Theory and Psychophysics* (Wiley, 1966).
29. Rubner, Y., Tomasi, C. & Guibas, L.J. The Earth Mover's Distance as a metric for image retrieval. *Int. J. Comput. Vis.* **40**, 99–121 (2000).
30. Maunsell, J.H. & van Essen, D.C. The connections of the middle temporal visual area (MT) and their relationship to a cortical hierarchy in the macaque monkey. *J. Neurosci.* **3**, 2563–2586 (1983).
31. Boussaoud, D., Ungerleider, L.G. & Desimone, R. Pathways for motion analysis: cortical connections of the medial superior temporal and fundus of the superior temporal visual areas in the macaque. *J. Comp. Neurol.* **296**, 462–495 (1990).
32. Greenblatt, S.H. Alexia without agraphia or hemianopsia. Anatomical analysis of an autopsied case. *Brain* **96**, 307–316 (1973).
33. Yeatman, J.D., Rauschecker, A.M. & Wandell, B.A. Brain & Language. *Brain Lang.* **125**, 146–155 (2013).
34. Kriegeskorte, N. *et al.* Human cortical object recognition from a visual motion flowfield. *J. Neurosci.* **23**, 1451–1463 (2003).
35. Orban, G.A. A motion area in human visual cortex. *Proc. Natl. Acad. Sci. USA* **92**, 993–997 (1995).
36. Braddick, O.J., O'Brien, J.M., Wattam-Bell, J., Atkinson, J. & Turner, R. Form and motion coherence activate independent, but not dorsal/ventral segregated, networks in the human brain. *Curr. Biol.* **10**, 731–734 (2000).
37. Colby, C.L., Duhamel, J.R. & Goldberg, M.E. Ventral intraparietal area of the macaque: anatomic location and visual response properties. *J. Neurophysiol.* **69**, 902–914 (1993).
38. Conturo, T.E. *et al.* Tracking neuronal fiber pathways in the living human brain. *Proc. Natl. Acad. Sci. USA* **96**, 10422–10427 (1999).
39. Mangin, J.F. *et al.* Toward global tractography. *Neuroimage* **80**, 290–296 (2013).
40. Aganj, I. *et al.* Medical image analysis. *Med. Image Anal.* **15**, 414–425 (2011).
41. Neher, P.F. *et al.* MITK global tractography. in *Proc. SPIE*, Vol. 8314 (eds. Haynor, D.R. & Ourselin, S.) (SPIE, 2012).
42. Jbabdi, S., Woolrich, M.W., Andersson, J.L.R. & Behrens, T.E.J. A Bayesian framework for global tractography. *Neuroimage* **37**, 116–129 (2007).
43. Sherbondy, A.J., Dougherty, R.F., Ananthanarayanan, R., Modha, D.S. & Wandell, B.A. Think global, act local; projectome estimation with BlueMatter. *Med. Image Comput. Comput. Assist. Interv.* **12**, 861–868 (2009).
44. Sherbondy, A.J., Dougherty, R.F., Ben-Shachar, M., Napel, S. & Wandell, B.A. ConTrack: finding the most likely pathways between brain regions using diffusion tractography. *J. Vis.* **8**, 15 (2008).
45. Schreiber, J., Riffert, T., Anwander, A. & Knösche, T.R. Plausibility tracking: A method to evaluate anatomical connectivity and microstructural properties along fiber pathways. *Neuroimage* **90**, 163–178 (2014).
46. Parker, G.J.M. *et al.* Initial demonstration of *in vivo* tracing of axonal projections in the macaque brain and comparison with the human brain using diffusion tensor imaging and fast marching tractography. *Neuroimage* **15**, 797–809 (2002).
47. Seehaus, A.K. *et al.* Histological validation of DW-MRI tractography in human postmortem tissue. *Cereb. Cortex* **23**, 442–450 (2013).
48. Jones, D.K., Knosche, T.R. & Turner, R. White matter integrity, fiber count, and other fallacies: the do's and don'ts of diffusion MRI. *Neuroimage* **73**, 239–254 (2013).
49. Fillard, P. *et al.* NeuroImage quantitative evaluation of 10 tractography algorithms on a realistic diffusion MR phantom. *Neuroimage* **56**, 220–234 (2011).
50. Assaf, Y. *et al.* The CONNECT project: combining macro- and micro-structure. *Neuroimage* **80**, 273–282 (2013).
51. Close, T.G. *et al.* A software tool to generate simulated white matter structures for the assessment of fibre-tracking algorithms. *Neuroimage* **47**, 1288–1300 (2009).
52. Mezer, A. *et al.* Quantifying the local tissue volume and composition in individual brains with magnetic resonance imaging. *Nat. Med.* **19**, 1667–1672 (2013).

## ONLINE METHODS

**STN96 and STN150 data sets: diffusion-weighted MRI acquisition.** Magnetic resonance imaging (MRI) diffusion-weighted data (DWI) were collected at Stanford's Center for Cognitive and Neurobiological Imaging (http://cni.stanford.edu/). We collected data in six males (age 37–39) using a 3-T General Electric Discovery 750 (General Electric Healthcare) equipped with a 32-channel head coil (Nova Medical). Data collection procedures were approved by the Stanford University Institutional Review Board. Written consent was collected from each participant.

Stanford 96 diffusion directions data set (STN96): for six subjects, we acquired two diffusion-weighted scans within a single scan session. Water diffusion was measured at 96 different directions across the surface of a sphere as determined by the electrostatic repulsion algorithm[53]. In all subjects, data were acquired at 1.5-mm$^3$ spatial resolution, and diffusion gradient strength was set to 2,000 s/mm$^2$ (TE = 96.8 ms). We used dual-spin echo diffusion-weighted sequences with full head coverage. Individual data sets were acquired with using two excitations ($n_{ex}$ = 2) that were averaged in $k$-space. We obtained ten non-diffusion-weighted ($b$ = 0) images at the beginning of each data set. The signal-to-noise ratio calculated over repeats of the nondiffusion images was greater than 20 in all data sets.

Stanford 150 diffusion directions data set (STN150): for one subject we acquired multiple data sets with 150 directions at 2-mm$^3$ spatial resolution and $b$ values of 1,000, 2,000 and 4,000 s/mm$^2$ (TE = 83.1, 93.6, and 106.9 ms).

MRI images for STN96 and STN150 were corrected for spatial distortions due to $B_0$ field inhomogeneity. To do so, we measured the $B_0$ magnetic field maps. Field maps were collected in the same slices as the functional data using a 16-shot, gradient-echo spiral-trajectory pulse sequence. Two volumes were successively acquired, one with TE set to 9.091 ms and the other with TE increased by 2.272 ms, and the phase difference between the volumes was used as an estimate of the magnetic field. To track slow drifts in the magnetic field (for example, due to gradient heating), we collected field maps before, after and between the two diffusion scans.

Subjects' motion was corrected using a rigid-body alignment algorithm[54]. Diffusion gradients were adjusted to account for the rotation applied to the measurements during motion correction. The dual-spin echo sequence we used does not require eddy current correction because it has a relatively long delay between the RF excitation pulse and image acquisition. This allows for sufficient time for the eddy currents to dephase. Preprocessing algorithms are publicly available as part of the Vistasoft software distribution (https://github.com/vistalab/vistasoft/).

**HCP90 data set.** We used seven brains with DWI data downloaded from https://www.humanconnectome.org/data/ (ref. 55). Measurements from the 2,000-s/mm$^2$ shell were extracted from the original data and were used for further analyses. Processing methods described in the following articles are applied to all HCP open-access preprocessed diffusion data[56].

**Anatomical MRI acquisition and tissue segmentation.** The white matter–gray matter border was defined using a 0.7-mm$^3$ T1-weighted FSPGR image. White matter–gray matter tissue contrast was increased by averaging two T1 measurements acquired in the same scan session. An initial segmentation was performed using an automated procedure (FreeSurfer[57]) and refined manually (http://www.itksnap.org/pmwiki/pmwiki.php).

**Generating whole-brain connectomes and tracts.** Fiber tracking was performed using MRtrix[16]. Diffusion-weighted images were motion compensated and aligned to the high-resolution T1-weighted anatomical images. The total white-matter volume was identified from the cortical segmentation (see above) and resampled at the resolution of the diffusion data. The white-matter volume was used as the seed region for fiber tracking. We tested two tracking methods implemented within MRtrix: (i) tensor-based deterministic tractography[16,23,24], a method that requires fitting a tensor at each voxel and tracking using the principal diffusion direction identified from the tensor, and (ii) CSD-based probabilistic tracking[16,25,26]. We tested a range of maximum harmonic orders ($L_{max}$ = 6–12), which determines the maximum number of deconvolution kernels used to estimate the fiber orientation distribution function (fODF) at each voxel by the CSD model (step size: 0.2 mm; minimum radius of curvature, 1 mm; maximum length, 200 mm; minimum length, 10 mm; fODF amplitude cutoff, 0.1). Results were qualitatively similar across the $L_{max}$ values.

For each tractography method, data set (STN150 $b$ value of 1,000, 2,000 or 4,000 s/mm$^2$ with 150 directions; STN96 $b$ value of 2,000 s/mm$^2$ with 96 directions; and HCP90 $b$ value of 2,000 s/mm$^2$ with 90 directions) and subject, we created one whole-brain connectome with 500,000 fascicles each. We repeated the analysis independently for each brain in each data set. Connectomes for the HCP90 data set were restricted to the posterior portion of each brain (occipital, parietal and temporal lobe as well as the cerebellum). For some analyses on the STN150 data set (**Supplementary Figs. 4** and **7**), we used three connectomes restricted to the left occipital lobe to build independent LiFE models and repeated our analyses in each one of these three connectomes. This allowed us to test the robustness of the results within a single brain given by (i) the stochasticity of the placement of the seed within the total white-matter volume to initiate fiber tracking and (ii) the stochasticity introduced by the probabilistic tracking algorithm in generating a connectome. As reported in the Results and **Supplementary Figures 3**, **4** and **7** (see error bars), results were quantitatively indistinguishable across repeated tracking and fitting of LiFE models.

**Segmentation and visualization.** To identify connections between different brain regions (hMT+, superior parietal gyrus, and primary visual cortex, **Supplementary Figs. 8** and **9**), we did the following. (i) We performed a whole-brain automatic parcellation using FreeSurfer[58]. (ii) We used the cortical regions for primary visual cortex (V1) and hMT+ using the cortical regions provided by FreeSurfer[59] by transforming them to the space of the diffusion data. (iii) We expanded these regions to cover portions of the white matter adjacent to each cortical area by applying a three-dimensional Gaussian smoothing with a spatial kernel of 3 mm$^3$. (iv) We identified the fascicles in the whole-brain connectome with termination (end points) inside these expanded ROIs. (v) The anterior commissure was identified manually in each subject from the high-resolution anatomical image. We selected

fascicles that intersected a 5-mm-diameter sphere centered at the location of the anterior commissure. We segmented the major white-matter fascicles using AFQ[3]. Tracts and brain images were generated using Matlab Brain Anatomy (MBA) https://github.com/francopestilli/mba/.

**Predicting the diffusion signal within a voxel.** A complete diffusion MRI experiment measures brain volumes with and without diffusion sensitization. Diffusion sensitization (a combination of diffusion gradient strength, duration of the diffusion gradient and the interval between the pulses of the diffusion gradient) is denoted as $b$. We represent direction as a three-dimensional, unit-length, column vector.

Suppose the nondiffusion signal at a voxel is $S_0$ and the diffusion signal in the direction $\theta$ and the presence of a gradient, $b$, is $S(\theta,b)$. The diffusion signal in a particular direction using a specific gradient strength ($b$) is specified using the following equation[60]

$$S(\theta,b) = S_0 e^{-bA(\theta)} \quad (1)$$

where $A(\theta)$ is the apparent diffusion coefficient in the direction $\theta$. For a simple shape, such as an idealized cylinder that represents a short segment of a fascicle, $f$, the apparent diffusion coefficients in different directions can be summarized by the quadratic formula[61]

$$A_f(\theta) = \theta^t Q \theta \quad (2)$$

Equation (2) states that for a single small segment of a fascicle, the apparent diffusion in any direction can be computed using a matrix $Q$, whose entries depend on the local fascicle orientation. The matrix is a $3 \times 3$ positive-definite quadratic form, which means that there is an invertible matrix $M$ such that $Q = M^t M$. It follows that $Q$ is symmetric and $\theta^t Q \theta > 0$.

The expected diffusion in a specific voxel, $v$, completely filled by one fascicle, $f$, is

$$S_v(\theta,b) = S_0 e^{-bA_f(\theta)} \quad (3)$$

An important special case is the purely isotropic compartment, $A_0$, (i.e., equal diffusion in all directions, $\theta$). This corresponds, for example, to the portion of the voxel containing cerebrospinal fluids, astrocytes and other tissue. A typical voxel is likely to contain a combination of fascicles and these isotropic tissues. We express the predicted diffusion signal from a single voxel as the weighted sum of the contributions from the fascicles in the compartment and the isotropic term

$$S_v(\theta,b) = w_0 S_0 e^{-bA_0} + \sum_{f \in v} w_f S_0 e^{-bA_f(\theta)} \quad (4)$$

We can rewrite equation (4), the diffusion in a voxel, as the sum of an isotropic term and the sum of orientation-dependent functions from each fascicle

$$S_v(\theta,b) = I_v + \sum_{f \in v} w_f O_f(\theta) \quad (5)$$

The isotropic term, $I_v$, is simply the mean diffusion signal in the voxel

$$I_v = \frac{1}{N_\theta} \sum_\theta S_v(\theta,b) \quad (6)$$

The fascicle-specific function, $O_f(\theta)$, is anisotropic with zero mean. It describes the modulation of the diffusion signal around its mean.

$$O_f(\theta) = S_0 \left( e^{-bA_f(\theta)} - \frac{1}{N_\theta} \sum_\theta e^{-bA_f(\theta)} \right) \quad (7)$$

The fascicle weights in a voxel are estimated by first subtracting $I_v$ from the diffusion signal and then solving the linear equation for the values, $w_f$, that minimize

$$\sum_\theta \left( (S_v(\theta,b) - I_v) - \sum_{f \in v} w_f O_f(\theta) \right)^2, \text{ subject to } w_f \geq 0 \quad (8)$$

The difference between the measured diffusion signal and the mean diffusion signal is

$$M(\theta,v) = S_v(\theta,b) - I_v \quad (9)$$

The predicted signal modulation based on the fascicles in $v$ is

$$P(\theta,v) = \sum_{f \in v} w_f O_f(\theta) \quad (10)$$

**Estimating fascicle weights from the connectome.** Finally, we solve for the fascicle weights by minimizing the error across all the voxels in the connectome, $C$. Specifically, we find $w_f$ that minimize the expression

$$\text{argmin}_{w_f} \sum_{v \in C} \sum_\theta (M(\theta,v) - P(\theta,v))^2, w_f \geq 0$$

or, equivalently,

$$\text{argmin}_{w_f} \sum_{v \in C} \sum_\theta \left( M(\theta,v) - \sum_{f \in v} w_f O_f(\theta) \right)^2, w_f \geq 0 \quad (11)$$

**Supplementary Figure 2b** shows equation (11) in matrix tableau. We solve for the non-negative weights using the algorithm defined in ref. 15.

There are many possible variants of this formulation. For example, it is possible to impose additional minimization constraints (for example, sparsity or uniformity on the weights), or even to allow the weights to vary along the fascicle path.

In summary, the connectome model is expressed as a minimization with respect to a large set of linear equations (equation (11)). The matrix representing the connectome model is sparse,





doi:10.1038/nmeth.3098

and for our high-resolution data sets, the matrix row size is $(N_v \times N_\theta)$: about 7,000,000 for the STN150 data set and 40,000,000 for the STN96 data set. The matrix begins with a column size $(N_f)$ of about 500,000 fascicles in the candidate connectome. The column dimension is reduced when the optimized connectome is reached. See **Supplementary Figure 2** for details on the matrix representation of the linear model for the connectome.

Software implementation of the method is provided at https://francopestilli.github.io/life/ and as **Supplementary Software**. Sample data is provided at http://purl.stanford.edu/cs392kv3054.


53. Jones, D.K., Horsfield, M.A. & Simmons, A. Optimal strategies for measuring diffusion in anisotropic systems by magnetic resonance imaging. *Magn. Reson. Med.* **42**, 515–525 (1999).
54. Friston, K.J. *et al.* Spatial registration and normalization of images. *Hum. Brain Mapp.* **3**, 165–189 (1995).
55. Van Essen, D.C. *et al.* The Human Connectome Project: a data acquisition perspective. *Neuroimage* **62**, 2222–2231 (2012).
56. Van Essen, D.C. *et al.* The WU-Minn Human Connectome Project: an overview. *Neuroimage* **80**, 62–79 (2013).
57. Fischl, B. FreeSurfer. *Neuroimage* **62**, 774–781 (2012).
58. Destrieux, C., Fischl, B., Dale, A. & Halgren, E. Automatic parcellation of human cortical gyri and sulci using standard anatomical nomenclature. *Neuroimage* **53**, 1–15 (2010).
59. Fischl, B. *et al.* Cortical folding patterns and predicting cytoarchitecture. *Cereb. Cortex* **18**, 1973–1980 (2008).
60. Stejskal, E.O. & Tanner, J.E. Spin diffusion measurements: spin echoes in the presence of a time-dependent field gradient. *J. Chem. Phys.* **42**, 288 (1965).
61. Basser, P.J. & Pierpaoli, C. Microstructural and physiological features of tissues elucidated by quantitative-diffusion-tensor MRI. *J. Magn. Reson. B.* **111**, 209–219 (1996).